ADVANCED FUNCTIONAL MATERIALS
www.afm-journal.de

Strain Sensors with a High Sensitivity and a Wide Sensing Range Based on a $Ti_3C_2T_x$ (MXene) Nanoparticle–Nanosheet Hybrid Network

Yina Yang, Liangjing Shi, Zherui Cao, Ranran Wang, and Jing Sun**

A high sensitivity and large stretchability are desirable for strain sensors in wearable applications. However, these two performance indicators are contradictory, since the former requires a conspicuous structural change under a tiny strain, whereas the latter demands morphological integrity upon a large deformation. Developing strain sensors with both a high sensitivity (gauge factor (GF) > 100) and a broad strain range (>50%) is a considerable challenge. Herein, a unique $Ti_3C_2T_x$ MXene nanoparticle–nanosheet hybrid network is constructed. The migration of nanoparticles leads to a large resistance variation while the wrapping of nanosheet bridges the detached nanoparticles to maintain the connectivity of the conductive pathways in a large strain region. The synergetic motion of nanoparticles and nanosheets endows the hybrid network with splendid electrical–mechanical performance, which is reflected in its high sensitivity (GF > 178.4) over the entire broad range (53%), the super low detection limit (0.025%), and a good cycling durability (over 5000 cycles). Such high performance endows the strain sensor with the capability for full-range human motion detection.

1. Introduction

In recent years, stretchable and wearable strain sensors have attracted great attention in the research community due to their advantages, including portability, foldability, lightweight, and biocompatibility.[1–10] Sensitivity (i.e., gauge factor (GF)) and stretchability are two crucial parameters used to evaluate the sensing performance of strain sensors. A high sensitivity is required for subtle deformations, such as the pulse and heartbeat. Meanwhile, a high stretchability is fundamental for detecting substantial body motions induced by joint movements. In general, to meet the basic requirements of full-range human motion detection, it is essential for a strain sensor to have a sensing range over 50% and a gauge factor larger than 100 in the full working range simultaneously.[11] However, enhancements in sensitivity and working range are contradictory because the sensitivity requires a significant structural change under a small strain, while stretchability requires the device to maintain the connectivity of conductive pathways in a large strain region; thus, the fabrication of an ideal strain sensor still faces great challenges.

To make a strain sensor exhibit a desirable sensitivity in a broad sensing range, two strategies are commonly used. One important consideration is to manipulate the architecture design of sensing materials and substrates, for example, by introducing microarrays,[12–15] wrinkles,[16] and cracks.[17–19] However, orchestrating such a sophisticated geometrical architecture may increase the complexity of the craftsmanship. Another strategy is to synthesize new conductive materials and tune their microstructures to enhance the sensing performance. Generally, a strain sensor made of a 1D material always exhibits a large working range but a poor sensitivity, since 1D materials with a high aspect ratio can maintain good interconnection while manifesting inconspicuous resistance changes under an extended strain range.[1,2,20–24] Conversely, strain sensors based on 2D materials demonstrate good sensitivity but suffer from low stretchability and stability, which may be related with the low aspect ratio of 2D materials.[15,25–29] Recent research has suggested that the strong interaction (i.e., hydrogen bonds or van der Waals forces) between adjacent sheets may play a critical role in narrowing the working range, which obstructs the effective slippage between the sheets so that the 2D materials are inclined to rapidly split into scales and cut off the conductive pathways during the tensile process. Cai et al. and Shi et al. introduced joint materials or lubricants into the 2D materials to promote the slippage of the sheets and reduce the generation of cracks, which considerably improved the comprehensive performance of the sensors (the sensitivities reached 772.6 and 2392.9 respectively, and the working ranges reached 70% and 62%, respectively). Nevertheless, these studies still did not achieve a gauge factor over 100 for the entire range.[11,38] Controlling the microstructures to promote effective slipping of sensing units while avoiding the formation of large cracks may be an ideal solution to broaden the working range of sensors based on 2D materials without sacrificing their sensitivity. However, constructing a desirable

Dr. Y. Yang, Dr. L. Shi, Dr. Z. Cao, Dr. R. Wang, Prof. J. Sun
State Key Laboratory of High Performance Ceramics and Superfine Microstructure
Shanghai Institute of Ceramics
Chinese Academy of Sciences
Shanghai 200050, China
E-mail: wangranran@mail.sic.ac.cn; jingsun@mail.sic.ac.cn
The ORCID identification number(s) for the author(s) of this article can be found under https://doi.org/10.1002/adfm.201807882.

DOI: 10.1002/adfm.201807882

composite structure is still arduous, and more attempts may be needed to develop of new materials.

MXenes, which refer to 2D early transition metal carbide or carbonitride, are a new type of graphene-like laminated material. Their chemical formula is $M_{n+1}X_nT_x$, and they can be obtained by selectively etching out element A from the parent MAX phase (n = 1, 2, and 3), M stands for early transition metal, A means an element from group 13 or 14, X represents carbon and/or nitrogen, T denotes the surface termination of MXenes, such as with OH, F, and O, and x is the number of surface termination).[30–32] MXenes have many merits, including a high conductivity, excellent mechanical properties, good oxidation resistance, as well as a controllable, low-cost manufacturing process, resulting in diverse applications, such as in energy storage devices, electromagnetic shielding, and sensors.[33–37] However, as strain sensing materials, MXenes also face the problem of a narrow stretching range because of the rapid crack propagation of stacked MXene sheets,[38] which considerably restricts the application of MXene-based sensors.

Herein, we successfully constructed a unique $Ti_3C_2T_x$ (a typical MXene material) nanoparticle–nanosheet hybrid network for strain sensors with a high sensitivity (GF > 178.4) over the full broad range (0–53%), a very low detection limit (0.025%), and a good cycling durability (over 5000 cycles). The synergetic motion of the $Ti_3C_2T_x$ nanoparticles and nanosheets was mainly responsible for the superb comprehensive performance. Three distinctive sensing stages and a constrained microcrack propagation mechanism were discovered. When stretched, the migration and detachment of the nanoparticles resulted in a large resistance variation, whereas the nanosheets wrapped and bridged the detached nanoparticles, which maintained the connectivity of the conductive pathways over a large strain region. The $Ti_3C_2T_x$ nanoparticles and nanosheets in the hybrid network with different ratios displayed diversity in structure and morphology, which assisted in fully functionalizing the microstructures and maximizing the synergistic effect. The $Ti_3C_2T_x$ hybrid network demonstrated considerable sensitivity for the sensors based on unitary nanoparticles or sheets, but it had a 7–10 times enlargement in the working range. Moreover, the demonstration of human activity detection from as subtle as accurate speech recognition to vigorous human motions confirmed the superiority of the hybrid network.

2. Results and Discussion

2.1. Morphology Analysis of $Ti_3C_2T_x$

Figure 1a schematically illustrates the fabrication of the $Ti_3C_2T_x$-based strain sensors that involved a chemical liquid etching method and a one-step transformation to achieve the desirable sensor architecture (see the Experimental Section for fabrication details). The morphology of $Ti_3C_2T_x$ can be controlled by employing different etchants (i.e., hydrofluoric acid (HF), tetramethylammonium hydroxide (TMAOH)[39]), etching time (i.e., 6, 18, or 24 h), and sonication (or handshaking) time (i.e., 20 min, 1 h, 2 h, 3 h, or 4 h). The final $Ti_3C_2T_x$ samples that were processed using various experimental conditions are referred to as "HF_y-d_z-$Ti_3C_2T_x$" and "TMA-$Ti_3C_2T_x$" (HF and TMA mean treatment with HF or TMAOH, y is the etching time, and z stands for the sonication time) that corresponds to the etchant, etching time, and sonication time. Figure 1b shows the X-ray diffraction (XRD) pattern of Ti_3AlC_2 and multilayer $Ti_3C_2T_x$ (m-$Ti_3C_2T_x$) obtained for the three different conditions. The disappearance of the (104) peak for the samples etched by HF for more than 6 h demonstrates the transformation of Ti_3AlC_2 into the accordion-like m-$Ti_3C_2T_x$ (Figure 1c,d). However, TMAOH only caused the majority of Ti_3AlC_2 to convert to the Ti_3C_2 phase, which appeared as a thick paper morphology (Figure 1e), and is very different from the HF-treated samples. In addition, the (002) peak of TMAOH-treated m-$Ti_3C_2T_x$ shifts to lower 2θ values in contrast to the HF-treated samples, implying a broader interspace for the former. The difference between the m-$Ti_3C_2T_x$ samples can be related to the different etching intensities. HF is able to trigger a violent reaction in a short time to complete the etching process, whereas TMAOH slightly attacks the Al layer, and the TMA^+ cation can gradually embed into the interface between the m-$Ti_3C_2T_x$ sheets during etching to expand the interlamellar distance.

Figure 1f–h (Figure S1, Supporting Information) shows the sizes of each sample as measured by atomic force microscopy (AFM). The $HF_{6\ h}$-$d_{3\ h}$-$Ti_3C_2T_x$ sample exhibits a thickness of 200 nm and a lateral size of 100–200 nm (Figure 1f), whereas the thickness of TMA-$Ti_3C_2T_x$ was measured to be 0.5 nm with a lateral size that is larger than 500 nm (Figure 1h). It can be seen that $HF_{6\ h}$-$d_{3\ h}$-$Ti_3C_2T_x$ is mainly composed of irregular nanoparticles, and most of the TMA-$Ti_3C_2T_x$ are monolayers. For $HF_{18\ h}$-$d_{20\ min}$-$Ti_3C_2T_x$, a large portion of the sample is as thick as 15 nm with a lateral size of 200–300 nm, which additionally demonstrates the irregular distribution of elongated snags that are thicker than 100 nm and thin layers with a lateral size of ≈1 µm (Figure 1g). Therefore, $HF_{18\ h}$-$d_{20\ min}$-$Ti_3C_2T_x$ can be considered a mixture of nanoparticles with diverse sizes and 2D stacked sheets.

Scanning electron microscope (SEM) images of the $Ti_3C_2T_x$ films confirmed the microstructure of the $Ti_3C_2T_x$ samples obtained under the different experimental conditions. As shown in **Figure 2**a, the $HF_{6\ h}$-$d_{3\ h}$-$Ti_3C_2T_x$ sample is mainly composed of nanoparticles. Despite the nanoparticles shown in the AFM images, larger grains (1–2 µm) were observed. When the etching time was prolonged to 18 h, the number of sheets increased with decreasing particle size; thus, a hybrid conductive network consisting of nanoparticles and nanosheets was successfully achieved (Figure 2b; Figure S2a, Supporting Information). However, further extension of the sonication time caused increasing quantity but decreasing lateral sizes of the sheets, resulting in a structural change from a nanoparticle–nanosheet hybrid network to 2D stacks (Figure 2c–f; Figure S2b,e, Supporting Information). AFM analysis confirmed the structure change, demonstrating a reduction in the lamellar thickness from 4.6 to 0.8 nm and in the lateral size from 850 to 350 nm (Figure S3, Supporting Information). In comparison, the TMA-$Ti_3C_2T_x$ conductive film (Figure 2g; Figure S2f, Supporting Information) is mostly composed of orderly stacked large-sized sheets with very few particles, and the surface of the film is smoother than other samples.

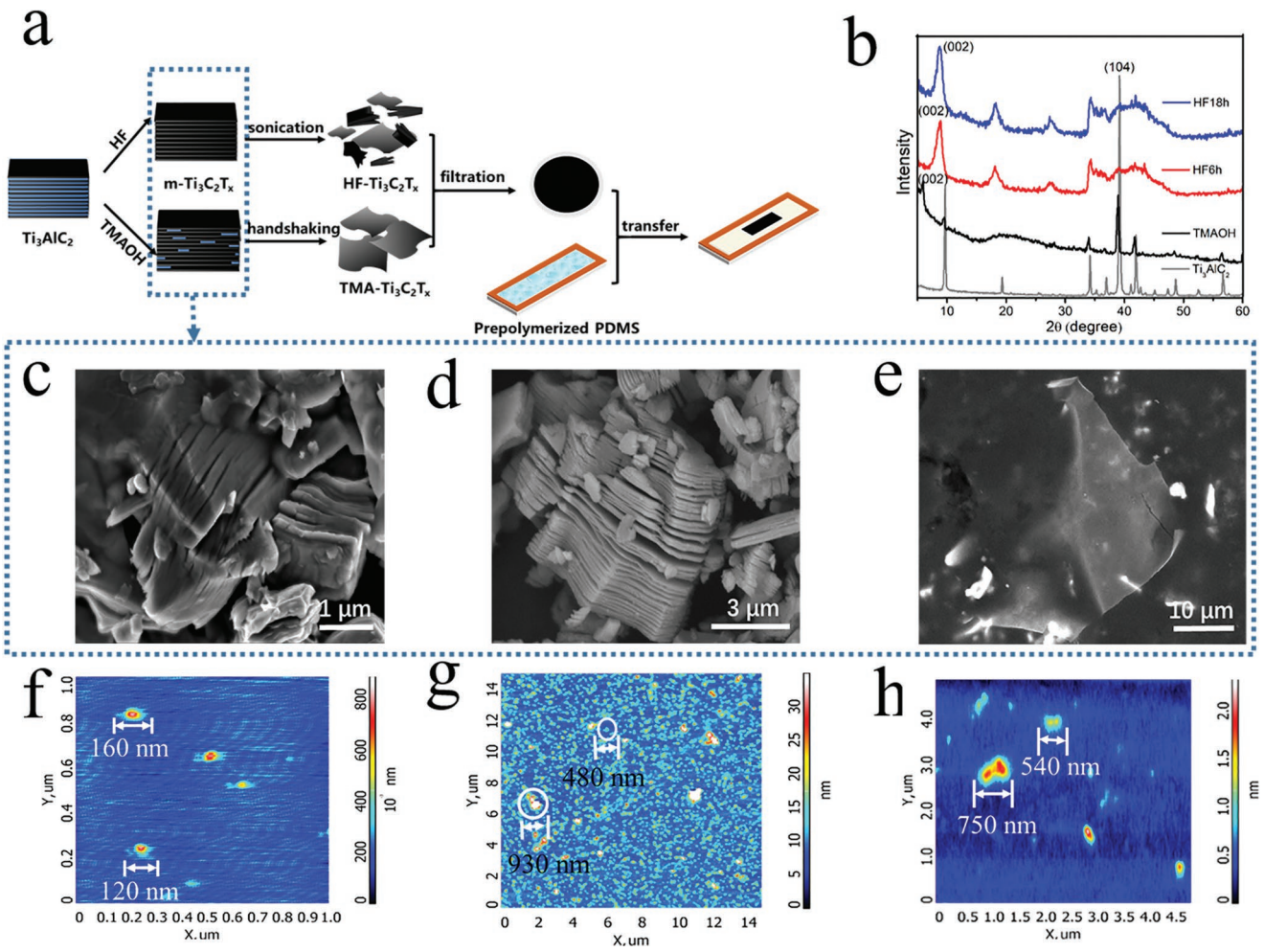

Figure 1. a) Fabrication process for the strain sensors based on $Ti_3C_2T_x$ with different morphologies. b) XRD pattern of m-$Ti_3C_2T_x$ and Ti_3AlC_2. SEM images of m-$Ti_3C_2T_x$ produced by c) HF for 6 h, d) HF for 18 h, and e) TMAOH for 24 h. AFM images of f) $HF_{6\ h}$-$d_{3\ h}$-$Ti_3C_2T_x$, g) $HF_{18\ h}$-$d_{20\ min}$-$Ti_3C_2T_x$, and h) TMA-$Ti_3C_2T_x$.

2.2. Sensing Performance Analysis

The electrical–mechanical performance of the strain sensors based on the $Ti_3C_2T_x$ network was investigated to determine the effect of the various structures of $Ti_3C_2T_x$. The similarity in thickness of all the $Ti_3C_2T_x$ films excludes the influence of film thickness, as shown in Figure 2h–i. A plot of the relative resistance variation ($\Delta R/R_0$, where ΔR is defined as (R–R_0), R is the electrical resistance under varying strains, and R_0 is the initial resistance) as a function of different strains was produced. The slope of the $\Delta R/R_0$–ε curve (given as GF) is in general used to evaluate the sensitivity of strain sensors. **Figure 3**a,b demonstrates the relative resistance variation of the strain sensors based on $Ti_3C_2T_x$ prepared by varying the etchants and etching time under an oriented tensile strain. Of note, regardless of the sensitivity or stretching range, there is a big difference in the three samples. The maximum working range of the strain sensor based on $HF_{6\ h}$-$d_{3\ h}$-$Ti_3C_2T_x$ is ≈5%, and the relative resistance variation–strain curve tends to be linear with a GF of 106.8. The quick disconnection between $Ti_3C_2T_x$ particles is likely responsible for the narrow response range. With regard to the TMA-$Ti_3C_2T_x$-based strain sensor, the value of GF under a strain of 0–3.7% is 142.7, which rapidly increases to 2495.3 within a small strain change (up to 4.8%). Although the sensitivity significantly increases by changing the morphology of $Ti_3C_2T_x$ from particles to sheets, a working range below 7% is still undesirable for many applications. By contrast, the $HF_{18\ h}$-$d_{20\ min}$-$Ti_3C_2T_x$-based strain sensor exhibits a sensing range of up to 53%, which is 7–10 times larger than $HF_{6\ h}$-$d_{3\ h}$-$Ti_3C_2T_x$- and TMA-$Ti_3C_2T_x$-based strain sensors and superior to most of the graphene-based strain sensors.[40–42] In addition to a wide sensing range, the $HF_{18\ h}$-$d_{20\ min}$-$Ti_3C_2T_x$-based strain sensor also demonstrates a high sensitivity with a GF of 178.4 within a strain range of 5%, a GF of 505.1 in the range of 5–35%, and a GF of 1176.7 in the range of 35–53%, indicating that the GF of the sensor is larger than 100 within the entire strain range and the working range is also above 50%. These parameters have been rarely achieved in previously reported studies (**Figure 4**; Table S1, Supporting Information).[11,15,38,43] As mentioned above, $HF_{18\ h}$-$d_{20\ min}$-$Ti_3C_2T_x$ can be considered to be a mixture of particles with diverse sizes and 2D stacked sheets. It is inferred that $Ti_3C_2T_x$

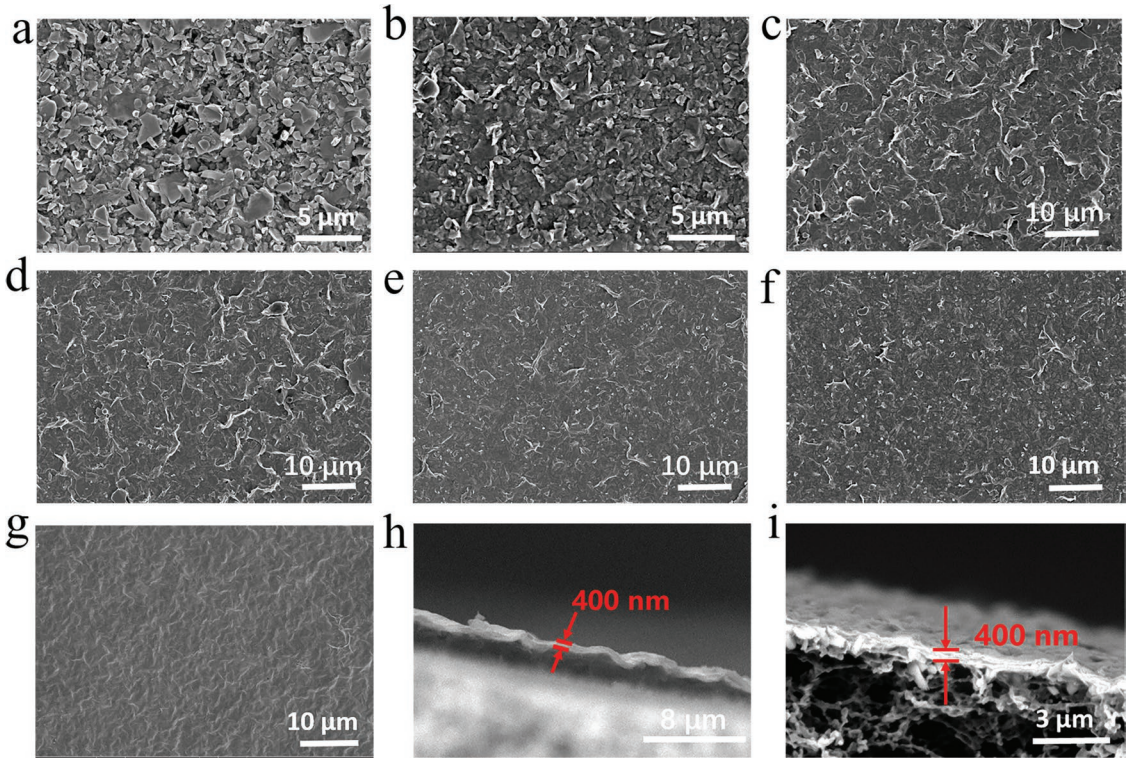

Figure 2. a) Top-view SEM images of the HF-$Ti_3C_2T_x$ conductive film with 6 h of etching and 3 h of sonication. b–f) Top-view SEM images of the HF-$Ti_3C_2T_x$ conductive film with 18 h of etching and 20 min, 1 h, 2 h, 3 h, and 4 h of sonication, respectively. g) Surface and h) cross-sectional SEM images of the TMA-$Ti_3C_2T_x$ conductive film. i) Cross-sectional SEM images of the HF-$Ti_3C_2T_x$ conductive film.

nanoparticles and sheets synergistically slide, resulting in a wide working range and a high sensitivity.

In addition to etchants and etching time, the sonication time also affected the sensing performance of the $Ti_3C_2T_x$-based strain sensors. As shown in Figure 3c,d, with the increase in sonication time, the shape of the relative resistance variation–strain curves significantly changed and grew exponentially, behaving similarly to the curve of the TMA-$Ti_3C_2T_x$-based strain sensor that exhibits a flat region and a short steep region. The maximum stretching range of the HF_{18h}-d_{1h}-$Ti_3C_2T_x$-, HF_{18h}-d_{2h}-$Ti_3C_2T_x$-, HF_{18h}-d_{3h}-$Ti_3C_2T_x$-, and the HF_{18h}-d_{4h}-$Ti_3C_2T_x$-based strain sensors decreased to 28%, 20%, 24%, and 21%, and the corresponding GFs within the flat region were 270.0 (0–20%), 384.5 (0–14%), 476.4 (0–13%), and 321.6 (0–16%), respectively. The steep regions were too nonlinear to measure the sensing performance.

The $HF_{18\ h}$-$d_{20\ min}$-$Ti_3C_2T_x$-based strain sensor was chosen as the testing sample in the following sections unless otherwise specified. Figure 3e shows the relative resistance variation with increasing step strain from 0.025% to 5% at a stretching rate of 60% min^{-1}, revealing that the detection limit of the $Ti_3C_2T_x$-based strain sensor is as low as 0.025%, and the variation in relative resistance appears to have a positive correlation with various strains; this matches the results shown in Figure 3a,b. The response time of the $Ti_3C_2T_x$-based strain sensor was determined by a real-time current–time curve as the sensor was stretched to a strain of 0.1% with a stretching speed of 40 mm s^{-1} (Figure 3f). Clearly, the response time was 130 ms, which is adequate for monitoring fast and instantaneous body motions. Figure 3g shows the frequency response of the $Ti_3C_2T_x$-based strain sensor at a frequency of 0.1–1 Hz under a strain of 10%. The shape and height of the current signal peaks at selected frequencies correspond with each other, which confirm the potency of the $Ti_3C_2T_x$-based strain sensor in high frequency motion recognition. The periodic shoulder peaks may be contributed to the vibration of the test instrument. The durability of the $Ti_3C_2T_x$-based strain sensor is demonstrated in Figure 3h. Clearly, there is no obvious degradation in the response signal that appears after 5000 stretching/releasing cycles under a 20% strain, demonstrating superior cycle stability and possible application in biomedical sensor technology.

2.3. Sensing Mechanism Analysis

To determine the underlying mechanism of the influence of the $Ti_3C_2T_x$ morphology, SEM characterization of the $Ti_3C_2T_x$-based strain sensors under various stretching states was conducted. **Figure 5** shows the microstructure variation of the $HF_{18\ h}$-$d_{20\ min}$-$Ti_3C_2T_x$-based strain sensor under applied strains (0–50%). Three distinctive stages can be recognized. Before stretching, the irregular nanoparticles and nanosheets were homogeneously interlaced without obvious holes, cracks, or oriented wrinkles on the conductive film (Figure 5a–c; Figure S4, Supporting Information). After a small range stretching (10%, stage I), a few holes generated by the migration of particles appeared on the film (Figure 5d–f). The random migration of $Ti_3C_2T_x$ nanoparticles directly resulted in a decrease in contact

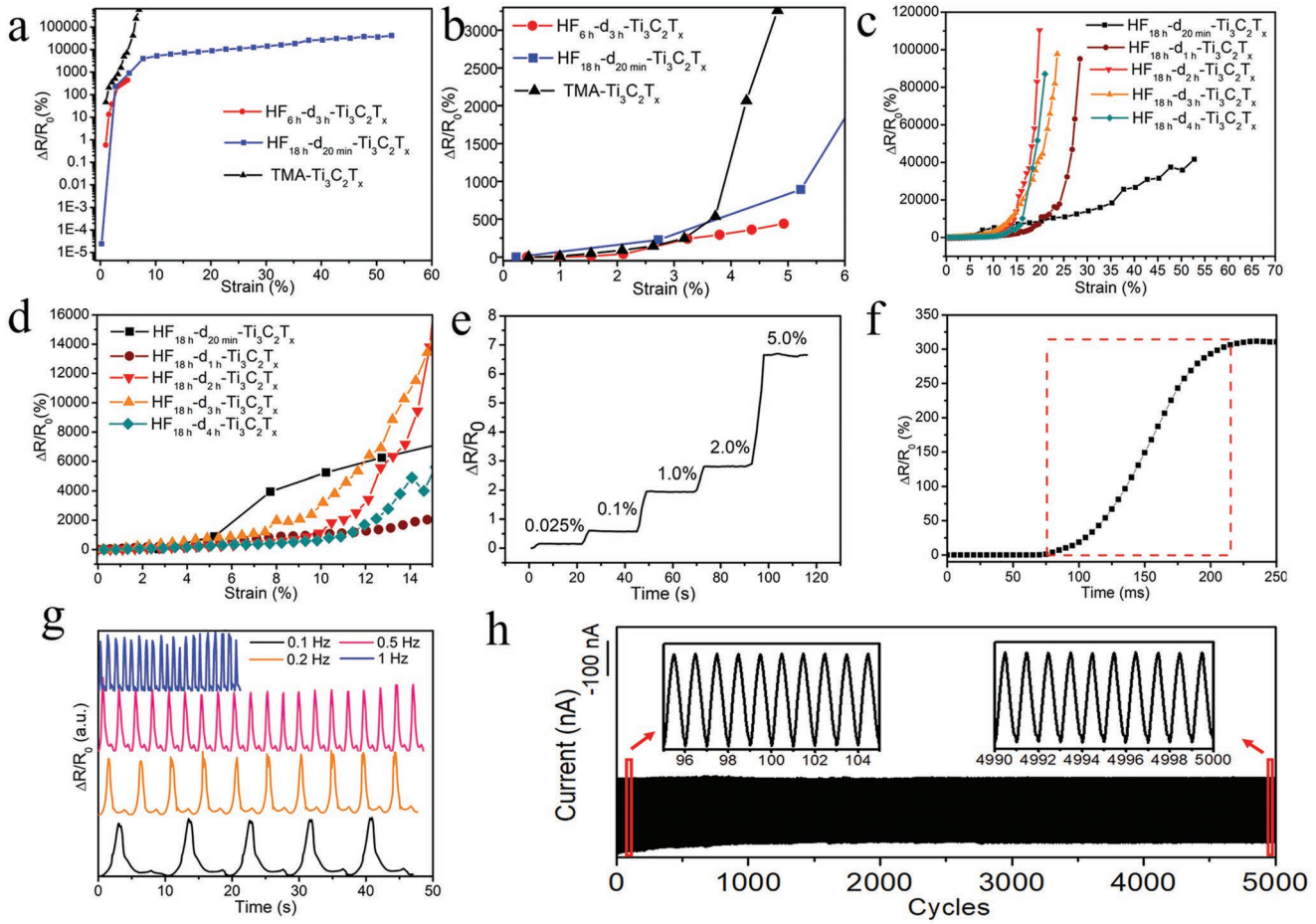

Figure 3. Strain sensing properties of the $Ti_3C_2T_x$-based strain sensors. a) Relative resistance variation–strain curve of the $Ti_3C_2T_x$-based strain sensors for various etchants and etching time (stretching rate of 60% min^{-1}). b) Reproduction of the curves in (a) within a 0–6% strain range. c) Relative resistance variation–strain curve of $Ti_3C_2T_x$-based strain sensors (treated with HF for 18 h) for various sonication time (the stretching rate was the same as in (a). d) Reproduction of the curves in (c) within a 0–15% strain range. e) Relative resistance variation under gradually increasing step strain from 0.025% to 5%. f) Real-time current–time response curve for the $Ti_3C_2T_x$-based strain sensor under a strain of 0.1% (stretching rate of 40 mm s^{-1}). g) Current signal changes of the strain sensor at selected frequencies under a 10% strain. h) Cycling durability curve of the strain sensor under a 20% strain (stretching rate of 60% min^{-1}).

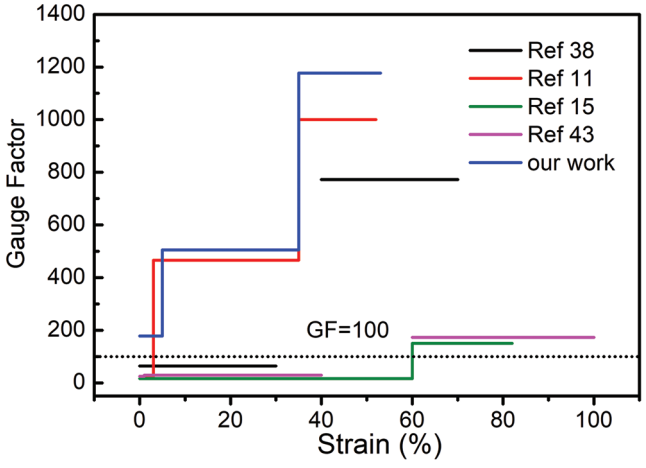

Figure 4. Comparison of the sensing performance of the $HF_{18\ h}$-$d_{20\ min}$-$Ti_3C_2T_x$-based strain sensors with recent studies.

area of conductive units and lead to an increase in resistance, and the generation of holes can effectively disperse the tensile stress, enhancing the stretchability of the strain sensor. Because of the randomness of particle migration, the change in the conductive pathways caused by the movement was larger than the plane slippage of the sheets; thus, the sensitivity of the strain sensor in the small strain range (0–5%) is outstanding, and the detection limit is as low as 0.025%. Moreover, the deformation of the sheets and their wrapping on the particles can be observed in Figure S5 in the Supporting Information. Evidently, there are some tiny wrinkles that arise on the sheets in this state, which are parallel to the tensile direction (Figure 5d). When further stretched (20%, stage II), the nanoparticles keep on isolating from each other, and the number of holes increases; meanwhile, the nanosheets are in a tighter state, and the wrinkles become more obvious (Figure 5g–i; Figure S6c, Supporting Information), which is due to the sheets further wrapping the particles to form conductive clusters (Figure S6d, Supporting Information). Moreover, some microcracks that

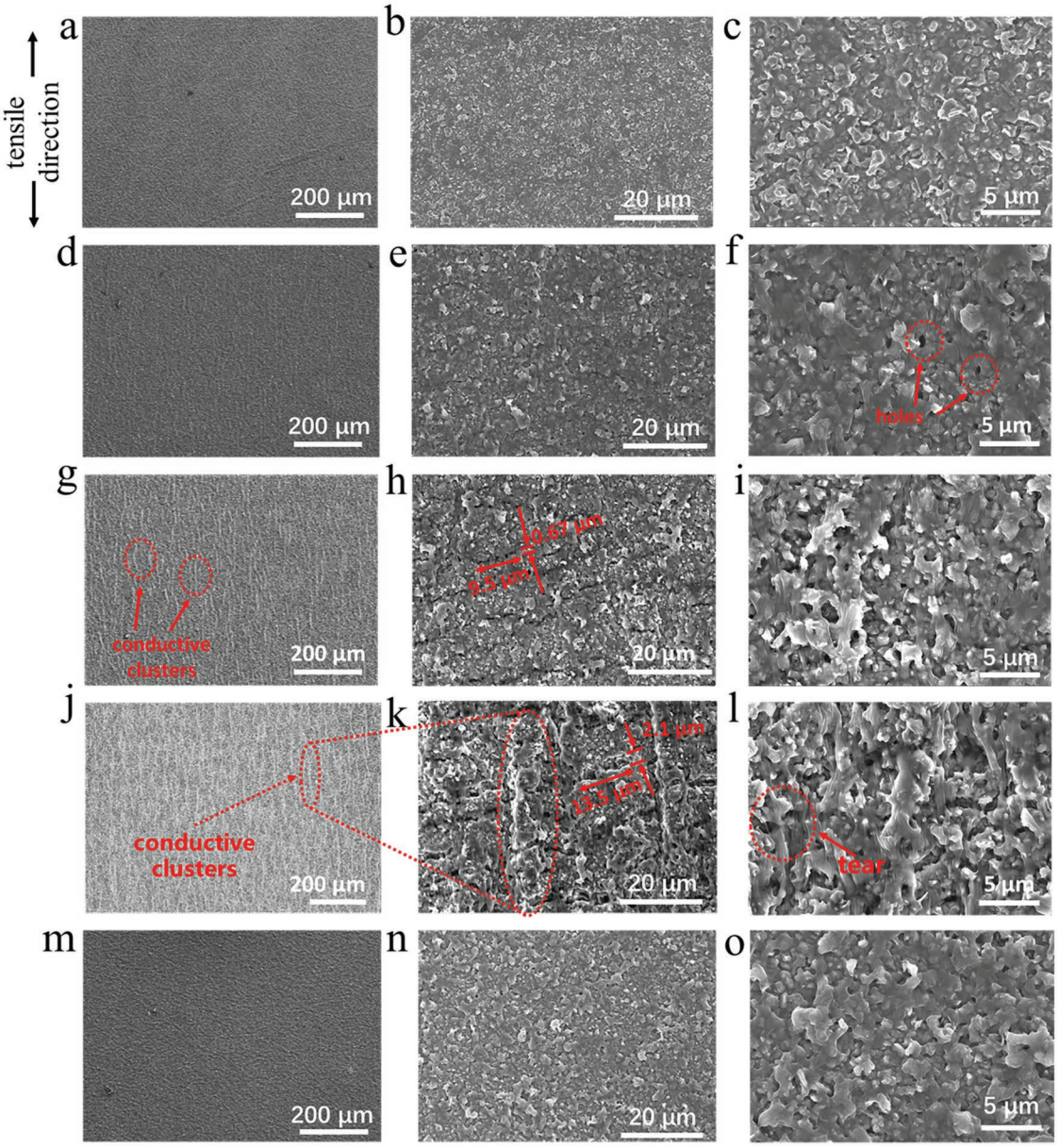

Figure 5. Top-view SEM images of the $HF_{18\ h}$-$d_{20\ min}$-$Ti_3C_2T_x$ conductive film at various stretching states during the first stretching–releasing cycle: a–c) 0%, d–f) 10%, g–i) 20%, j–l) 50%, and m–o) released to 0%.

are almost perpendicular to the tensile direction appear in the film (Figure S6a,b, Supporting Information), and their length is ≈10 μm with a width that is smaller than 1 μm. The crack ratio at this state is calculated from Figure S8a,b in the Supporting Information to be 1.08%. Obviously, the generation of microcracks can be responsible for the more rapid increase in the resistance within the second strain range. Figure 5j–l and Figure S7 in the Supporting Information depicts the morphology when the strain sensor is stretched to almost the limited working range (50% stage III). The sheets further wrap up the particles into bunch-like conductive clusters to construct a texture structure. The length of the transverse microcracks (≈13.5 μm) did not obviously grow compared with the 20% tensile sample; only the widths of the microcracks (about 2 μm) were enlarged by the simultaneous action of lateral extrusion and longitudinal stretching, and the crack ratio increased to 7.47% as shown in Figure S8c,d in the Supporting Information (since the gully caused by the lateral extrusion was also calculated as the crack area, the value was larger than the actual one). Therefore, we can reasonably speculate that the wrapping of the nanosheets on the particles and the bridging effect of the nanosheets on the cracks (Figure S7d, Supporting Information) effectively hinder the propagation of the cracks, keeping the size of the cracks very small in magnitude and maintaining the connection of the conductive pathways; thus, the sensing range of the strain sensor is considerably enhanced. This sensing mechanism can be called a constrained microcrack propagation mechanism. Moreover, the nanosheets that are

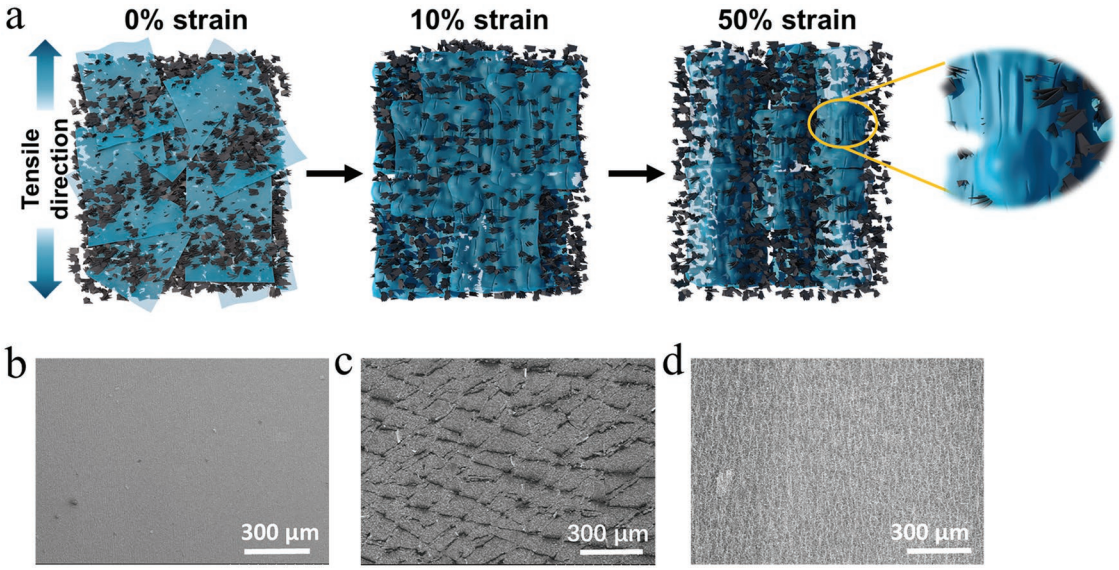

Figure 6. a) Schematic diagram of the $HF_{18\,h}$-$d_{20\,min}$-$Ti_3C_2T_x$ conductive film at various stretching states during the first stretching–releasing cycle. Top-view SEM images of b) $HF_{6\,h}$-$d_{3\,h}$-$Ti_3C_2T_x$-, c) TMA-$Ti_3C_2T_x$-, and d) $HF_{18\,h}$-$d_{20\,min}$-$Ti_3C_2T_x$-based strain sensors in the maximum tensile state.

shown in Figure 5l and Figure S7c (Supporting Information) were torn under exceeding strain, which contributes to the tremendous decrease in electrical conductance during the strain range of 35–53%. The synergetic motion of the $Ti_3C_2T_x$ nanoparticles and nanosheets is mainly responsible for the significant enhancement of the working range for the HF_{18h}-$d_{20\,min}$-$Ti_3C_2T_x$-based strain sensor. It is worth noting that the conductive network can almost return to the initial state without any cracks and wrinkles after the stress released (Figure 5m–o), which indicates that the stretching–releasing cycles are completely reversible, guaranteeing excellent cycling durability of the $HF_{18\,h}$-$d_{20\,min}$-$Ti_3C_2T_x$-based strain sensor.

The entire tensile process of the HF_{18h}-$d_{20\,min}$-$Ti_3C_2T_x$-based strain sensor is given in **Figure 6**a. In comparison, the SEM images of the first stretching–releasing process for the HF_{6h}-d_{3h}-$Ti_3C_2T_x$- and TMA-$Ti_3C_2T_x$-based strain sensors are shown in Figures S9 and S10 in the Supporting Information. The HF_{6h}-d_{3h}-$Ti_3C_2T_x$-based strain sensor lost conductance under a large strain, which may be due to the lack of enough sheets to form conductive clusters and bridge the conductive pathways. In addition, no obvious cracks were generated in the film regardless of the strain range (Figure 6b), and they were only accompanied by an increasing amount of holes, so that no abrupt conductance change was observed during the tensile process. By contrast, the large-sized sheets dominated the TMA-$Ti_3C_2T_x$-based strain sensor. During the tensile process, the tightly stacked sheets were inclined to produce huge cracks (the length was ≈200 μm and the width was ≈30 μm) to consume the stress rather than produce sheet slippage because of the strong interaction between adjacent sheets. As shown in Figure 6c and Figure S10 (Supporting Information), with increasing strain, scaly cracks appeared in the film and gradually expanded to obstruct the conductive pathways. Moreover, the cracks cannot be entirely repaired after strain released, which is unfavorable for the cycling stability of strain sensors. The strain sensors based on $HF_{18\,h}$-$d_{1\,h}$-$Ti_3C_2T_x$ and samples with a longer sonication time demonstrated a behavior similar to the TMA-$Ti_3C_2T_x$-based strain sensor (Figure S11, Supporting Information).

2.4. Human Activities Detection

The $Ti_3C_2T_x$-based strain sensor demonstrates outstanding sensing performance, including a high sensitivity, a wide stretching range, a low detection limit, and excellent durability, meaning it can be used as a wearable device for full-range human motion recognition. **Figure 7**a shows the current signal of a $Ti_3C_2T_x$-based strain sensor attached to the back of the hand. The electrical resistance regularly varied during the repeated fist clenching/unclenching process. When the $Ti_3C_2T_x$-based strain sensor was mounted on the knee joint, some large-scale body movements were recognized with different current signal curves, such as bending and walking (Figure 7b). In addition, due to high sensitivity and low detection limit of the $Ti_3C_2T_x$-based strain sensor, some complex and subtle human activities could also be identified. For instance, when the strain sensor was attached to the chest, the signal for breathing was clearly captured, and there were two distinct small peaks for each signal, which corresponded to the heartbeats (Figure 7c). In addition, as shown in Figure 7e, the $Ti_3C_2T_x$-based strain sensor is capable of precisely distinguishing different words either for with monosyllable alphabet, such as “a”, or for complex polysyllabic words, such as “sensor” and “MXene”, whose signal response curves exhibited one, two, and three tiny peaks, respectively. The characteristic signal of the human pulse is presented in Figure 7f. The three representative peaks corresponding to percussion (P), tidal (T), and diastolic (D) were all recognized, demonstrating the high sensitivity of the strain sensor. Moreover, in the case of noncontact, the strain sensor also successfully detected the signal of airflow generated by regular blowing (Figure 7g). Along these lines, our $Ti_3C_2T_x$-based

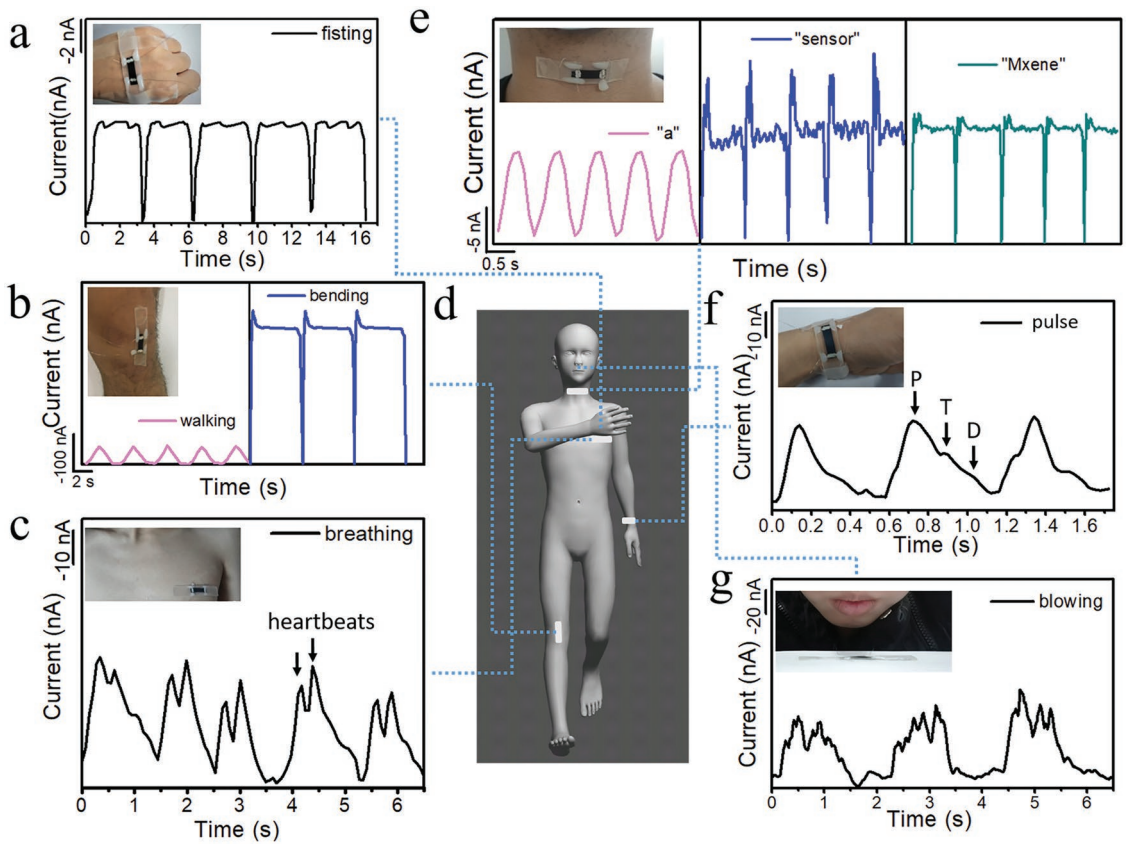

Figure 7. Response signal of the $Ti_3C_2T_x$-based strain sensor during monitoring of various physiological movements. a) Fisting. Inset: Photograph of a $Ti_3C_2T_x$-based strain sensor attached to the back of the hand. b) Walking and Knee bending. Inset: Photograph of a $Ti_3C_2T_x$-based strain sensor attached to the knee joint. c) Breathing. Inset: Photograph of a $Ti_3C_2T_x$-based strain sensor attached to the chest. d) A 3D mannequin. e) Speaking. Inset: Photograph of a $Ti_3C_2T_x$-based strain sensor attached to the throat. f) Pulse. Inset: Photograph of a $Ti_3C_2T_x$-based strain sensor attached to the wrist. g) Blowing. Inset: Photograph of blowing the $Ti_3C_2T_x$-based strain sensor.

strain sensor is a potential candidate for real-time human monitoring systems.

3. Conclusion

In summary, a stretchable strain sensor based on the $Ti_3C_2T_x$ MXene nanoparticle–nanosheet hybrid conductive network is presented that exhibits a high sensitivity (>178.4), a wide working range (0–53%), a low detection limit (0.025%), and outstanding cycling durability (over 5000 cycles). The demonstration of full-range human motion detection confirmed the high comprehensive performance of the hybrid network. The synergetic motion of the nanoparticles and nanosheets was discovered, and a constrained microcrack propagation mechanism is proposed. The migration of nanoparticles generated holes and microcracks, leading to a noteworthy variation in the resistance while the nanosheets wrapped and bridged the detached nanoparticles to constrain the rapid propagation of the microcracks. Although strain sensors based on a crack mechanism possess a high sensitivity, their working range is usually narrow since rapid propagation of cracks will significantly damage conducting paths. The constrained microcrack propagation mechanism proposed in this work may be an ideal solution to solve the problem and to enlighten the microstructure design of sensing materials and substrates.

4. Experimental Section

Synthesis of the HF-$Ti_3C_2T_x$ Suspension: $Ti_3C_2T_x$ was prepared by the most frequently used method of chemical liquid etching.[30] The precursor material Ti_3AlC_2 (200 meshes, Forsman Co., China) was selectively etched by the Al layer via HF (40 wt%), China National Medicines Corporation Ltd.) or TMAOH (Sigma). During the acid etching process, the Ti_3AlC_2 powder was slowly immersed into 40% HF at a ratio of 1 g:10 mL under continuous stirring for 6–18 h at room temperature. The resulting mixture was washed with distilled water and centrifuged until the pH was above 6. The precipitates were then collected by vacuum filtration and dried by a vacuum freeze dryer, to obtain multilayer $Ti_3C_2T_x$ powder. Next, 1 g of m-$Ti_3C_2T_x$ was added into 12 mL of dimethylsulfoxide (DMSO, China National Medicines Corporation Ltd.), and kept stirring the mixture for 18 h. Then, the DMSO was removed by centrifugal washing. Finally, the resulting sediment was added to 300 mL of distilled water, which was followed by 20 min to 4 h of sonication and 1 h of centrifugation at 3500 rpm. The supernatant containing delaminated $Ti_3C_2T_x$ (HF-$Ti_3C_2T_x$) was produced in the final step.

Synthesis of the TMA-$Ti_3C_2T_x$ Suspension: During the alkali etching process, Ti_3AlC_2 (1 g) powder was treated with 10 mL 20% HF under stirring (30 min) to remove surface oxidants of Ti_3AlC_2. The next

washing operation was similar to the acid etching process. First, 12 mL of 25% TMAOH was reacted with HF-treated Ti_3AlC_2 (1 g) for 24 h. The suspension was then washed and collected by centrifugation to obtain TMA-intercalated $Ti_3C_2T_x$. The sediment was dispersed in 300 mL of distilled water, delaminated by handshaking for 10 min, and centrifuged at 3500 rpm for 1 h to obtain the complete delaminated and large-scale $Ti_3C_2T_x$ (TMA-$Ti_3C_2T_x$).

Fabrication of $Ti_3C_2T_x$-Based Strain Sensors: A certain amount of as-prepared HF-$Ti_3C_2T_x$ and the TMA-$Ti_3C_2T_x$ suspension was vacuum filtered through a Millipore filter membrane to obtain $Ti_3C_2T_x$ conductive thin films. Initially, the concentration of the as-prepared HF-$Ti_3C_2T_x$ and TMA-$Ti_3C_2T_x$ was calibrated by the UV–vis spectrum to keep the same dosage of the $Ti_3C_2T_x$ suspension for each piece of conductive thin film. The resulting film was dried under vacuum at 25 °C for 12 h. Afterward, film was cut into rectangles with a size of 0.6 cm × 2.0 cm and was transferred to a polydimethylsiloxane (PDMS, Dow Corning) substrate. Components A and B of PDMS were mixed at a mass ratio of 10:1, magnetically stirred for 20 min, and placed in a vacuum oven for 10 min to remove bubbles. Afterward, PDMS was poured into a cuboid mold that was 80 mm × 15 mm × 1 mm and then was prepolymerized at 80 °C for 10 min. The tailored $Ti_3C_2T_x$ conductive film was transferred to prepolymerized PDMS with the conductive material downward. Then, the sample was placed in a drying oven at 80 °C for 1 h to finish the polymerization reaction of PDMS. The filter membrane coated on the conductive material could be dissolved by acetone in 30 min. Finally, silver electrodes were coated on both ends of the $Ti_3C_2T_x$ rectangle to complete the fabrication of the $Ti_3C_2T_x$-based strain sensors.

Characterization: The phase composition and crystalline structure of the samples were analyzed by a high-resolution multifunction X-ray diffractometer (D8 Discover Davinci, German). The morphologies were characterized by a field emission scanning electron microscope (S-4800, Hitachi, Japan). The concentration of the $Ti_3C_2T_x$ suspension was calibrated by using an UV–vis spectrophotometer (PerkinElmer Lambda 950, USA). The size distribution of the $Ti_3C_2T_x$ suspension was obtained by an atomic force microscope (NTEGRA, NT-MDT, Russia). The strain sensing tests were conducted by applying a high-precision electronic universal testing machine (CMT6103, MTS Systems, China) with a tensile controller and a software system. The resistance variation was determined by using an electrochemical workstation (PARSTAT 2273, Princeton Applied Research) by applying a constant voltage (0.1 V) on the two sides of the strain sensor to obtain a real-time current signal.

Supporting Information

Supporting Information is available from the Wiley Online Library or from the author.

Acknowledgements

This work was supported by the Shanghai Key Basic Research Project (Grant No. 16JC1402300), the National Natural Science Foundation of China (Grant No.61871368), the Youth Innovation Promotion Association CAS, the Shanghai Science and Technology Rising Star Project (17QA1404700), and the Young Elite Scientists Sponsorship Program by CAST. Instrument and equipment development program was sponsored by CAS (YJKYYQ20180065).

Conflict of Interest

The authors declare no conflict of interest.

Keywords

controllable synthesis, flexible and wearable, microcrack propagation mechanism, strain sensors, $Ti_3C_2T_x$

Received: November 6, 2018
Revised: January 30, 2019
Published online: February 15, 2019

[1] I. Kang, M. J. Schulz, J. H. Kim, V. Shanov, D. Shi, *Smart Mater. Struct.* **2006**, *15*, 737.
[2] T. Yamada, Y. Hayamizu, Y. Yamamoto, Y. Yomogida, A. Izadi-Najafabadi, D. N. Futaba, K. Hata, *Nat. Nanotechnol.* **2011**, *6*, 296.
[3] N. Lu, C. Lu, S. Yang, J. Rogers, *Adv. Funct. Mater.* **2012**, *22*, 4044.
[4] M. Amjadi, A. Pichitpajongkit, S. Lee, S. Ryu, I. Park, *ACS Nano* **2014**, *8*, 5154.
[5] C. Pang, C. Lee, K.-Y. Suh, *J. Appl. Polym. Sci.* **2013**, *130*, 1429.
[6] M. Amjadi, K.-U. Kyung, I. Park, M. Sitti, *Adv. Funct. Mater.* **2016**, *26*, 1678.
[7] T. Q. Trung, N. E. Lee, *Adv. Mater.* **2016**, *28*, 4338.
[8] A. Chortos, J. Liu, Z. Bao, *Nat. Mater.* **2016**, *15*, 937.
[9] T. Yang, D. Xie, Z. Li, H. Zhu, *Mater. Sci. Eng., R* **2017**, *115*, 1.
[10] T. Giorgino, P. Tormene, F. Lorussi, D. De Rossi, S. Quaglini, *IEEE Trans. Neural Syst. Rehabil. Eng.* **2009**, *17*, 409.
[11] X. Shi, S. Liu, Y. Sun, J. Liang, Y. Chen, *Adv. Funct. Mater.* **2018**, *28*, 1800850.
[12] C. Pang, J. H. Koo, A. Nguyen, J. M. Caves, M. G. Kim, A. Chortos, K. Kim, P. J. Wang, J. B. Tok, Z. Bao, *Adv. Mater.* **2015**, *27*, 634.
[13] J. Park, Y. Lee, J. Hong, M. Ha, Y. D. Jung, H. Lim, S. Y. Kim, H. Ko, *ACS Nano* **2014**, *8*, 4689.
[14] T. Q. Trung, S. Ramasundaram, B. U. Hwang, N. E. Lee, *Adv. Mater.* **2016**, *28*, 502.
[15] H. Park, Y. R. Jeong, J. Yun, S. Y. Hong, S. Jin, S.-J. Lee, G. Zi, J. S. Ha, *ACS Nano* **2015**, *9*, 9974.
[16] Q. Liu, J. Chen, Y. Li, G. Shi, *ACS Nano* **2016**, *10*, 7901.
[17] T. Yang, X. Li, X. Jiang, S. Lin, J. Lao, J. Shi, Z. Zhen, Z. Li, H. Zhu, *Mater. Horiz.* **2016**, *3*, 248.
[18] Z. Liu, D. Qi, P. Guo, Y. Liu, B. Zhu, H. Yang, Y. Liu, B. Li, C. Zhang, J. Yu, B. Liedberg, X. Chen, *Adv. Mater.* **2015**, *27*, 6230.
[19] D. Kang, P. V. Pikhitsa, Y. W. Choi, C. Lee, S. S. Shin, L. Piao, B. Park, K. Y. Suh, T. I. Kim, M. Choi, *Nature* **2014**, *516*, 222.
[20] Y. Zheng, Y. Li, Z. Li, Y. Wang, K. Dai, G. Zheng, C. Liu, C. Shen, *Compos. Sci. Technol.* **2017**, *139*, 64.
[21] M. Amjadi, Y. J. Yoon, I. Park, *Nanotechnology* **2015**, *26*, 375501.
[22] L. Cai, L. Song, P. Luan, Q. Zhang, N. Zhang, Q. Gao, D. Zhao, X. Zhang, M. Tu, F. Yang, W. Zhou, Q. Fan, J. Luo, W. Zhou, P. M. Ajayan, S. Xie, *Sci. Rep.* **2013**, *3*, 3048.
[23] K. K. Kim, S. Hong, H. M. Cho, J. Lee, Y. D. Suh, J. Ham, S. H. Ko, *Nano Lett.* **2015**, *15*, 5240.
[24] C. S. Boland, U. Khan, H. Benameur, J. N. Coleman, *Nanoscale* **2017**, *9*, 18507.
[25] C. S. Boland, U. Khan, C. Backes, A. O'Neill, J. McCauley, S. Duane, R. Shanker, Y. Liu, I. Jurewicz, A. B. Dalton, J. N. Coleman, *ACS Nano* **2014**, *8*, 8819.
[26] N. Karim, S. Afroj, S. Tan, P. He, A. Fernando, C. Carr, K. S. Novoselov, *ACS Nano* **2017**, *11*, 12266.
[27] H. Cong, F. Yang, C. Xue, K. Yu, L. Zhou, N. Wang, B. Cheng, Q. Wang, *Small* **2018**, *14*, 1704414.
[28] Y. N. Wijaya, J. Kim, W. M. Choi, S. H. Park, M. H. Kim, *Nanoscale* **2017**, *9*, 11705.
[29] G.-H. Lim, N.-E. Lee, B. Lim, *J. Mater. Chem. C* **2016**, *4*, 5642.

[30] M. Naguib, M. Kurtoglu, V. Presser, J. Lu, J. Niu, M. Heon, L. Hultman, Y. Gogotsi, M. W. Barsoum, *Adv. Mater.* **2011**, *23*, 4248.
[31] M. Naguib, V. N. Mochalin, M. W. Barsoum, Y. Gogotsi, *Adv. Mater.* **2014**, *26*, 992.
[32] M. Naguib, O. Mashtalir, J. Carle, V. Presser, J. Lu, L. Hultman, Y. Gogotsi, M. W. Barsoum, *ACS Nano* **2012**, *6*, 1322.
[33] B. Anasori, M. R. Lukatskaya, Y. Gogotsi, *Nat. Rev. Mater.* **2017**, *2*, 16098.
[34] M. Ghidiu, M. R. Lukatskaya, M. Q. Zhao, Y. Gogotsi, M. W. Barsoum, *Nature* **2014**, *516*, 78.
[35] F. Shahzad, M. Alhabeb, C. B. Hatter, B. Anasori, S. M. Hong, C. M. Koo, Y. Gogotsi, *Science* **2016**, *353*, 1137.
[36] Z. Ling, C. E. Ren, M. Q. Zhao, J. Yang, J. M. Giammarco, J. Qiu, M. W. Barsoum, Y. Gogotsi, *Proc. Natl. Acad. Sci. USA* **2014**, *111*, 16676.
[37] Y. Ma, N. Liu, L. Li, X. Hu, Z. Zou, J. Wang, S. Luo, Y. Gao, *Nat. Commun.* **2017**, *8*, 1207.
[38] Y. Cai, J. Shen, G. Ge, Y. Zhang, W. Jin, W. Huang, J. Shao, J. Yang, X. Dong, *ACS Nano* **2018**, *12*, 56.
[39] J. Xuan, Z. Wang, Y. Chen, D. Liang, L. Cheng, X. Yang, Z. Liu, R. Ma, T. Sasaki, F. Geng, *Angew. Chem., Int. Ed.* **2016**, *55*, 14569.
[40] M. Hempel, D. Nezich, J. Kong, M. Hofmann, *Nano Lett.* **2012**, *12*, 5714.
[41] J. Zhao, G. Wang, R. Yang, X. Lu, M. Cheng, C. He, G. Xie, J. Meng, D. Shi, G. Zhang, *ACS Nano* **2015**, *9*, 1622.
[42] X. Li, R. Zhang, W. Yu, K. Wang, J. Wei, D. Wu, A. Cao, Z. Li, Y. Cheng, Q. Zheng, R. S. Ruoff, H. Zhu, *Sci. Rep.* **2012**, *2*, 870.
[43] C. Wang, K. Xia, M. Jian, H. Wang, M. Zhang, Y. Zhang, *J. Mater. Chem. C* **2017**, *5*, 7604.